The Astrophysical Journal, 953:187 (14pp), 2023 August 20 https://doi.org/10.3847/1538-4357/ace24c

Statistical Relationship between Long-duration High-energy Gamma-Ray Emission and Solar Energetic Particles

A. Bruno[1,2], G. A. de Nolfo[1], J. M. Ryan[3], I. G. Richardson[1,4], and S. Dalla[5]
[1] Heliophysics Division, NASA Goddard Space Flight Center, Greenbelt, MD, USA; alessandro.bruno-1@nasa.gov
[2] Department of Physics, Catholic University of America, Washington, DC, USA
[3] Space Science Center, University of New Hampshire, Durham, NH, USA
[4] Department of Astronomy, University of Maryland, College Park, MD, USA
[5] Jeremiah Horrocks Institute, University of Central Lancashire, Preston PR1 2HE, UK
Received 2023 April 10; revised 2023 June 20; accepted 2023 June 22; published 2023 August 17

Abstract

Large solar eruptions are often associated with long-duration γ-ray emission extending well above 100 MeV. While this phenomenon is known to be caused by high-energy ions interacting with the solar atmosphere, the underlying dominant acceleration process remains under debate. Potential mechanisms include continuous acceleration of particles trapped within large coronal loops or acceleration at coronal mass ejection (CME)-driven shocks, with subsequent back-propagation toward the Sun. As a test of the latter scenario, previous studies have explored the relationship between the inferred particle population producing the high-energy γ-rays and the population of solar energetic particles (SEPs) measured in situ. However, given the significant limitations on available observations, these estimates unavoidably rely on a number of assumptions. In an effort to better constrain theories of the γ-ray emission origin, we reexamine the calculation uncertainties and how they influence the comparison of these two proton populations. We show that, even accounting for conservative assumptions related to the γ-ray flare, SEP event, and interplanetary scattering modeling, their statistical relationship is only poorly/moderately significant. However, though the level of correlation is of interest, it does not provide conclusive evidence for or against a causal connection. The main result of this investigation is that the fraction of the shock-accelerated protons required to account for the γ-ray observations is >20%–40% for six of the 14 eruptions analyzed. Such high values argue against current CME-shock origin models, predicting a <2% back-precipitation; hence, the computed number of high-energy SEPs appears to be greatly insufficient to sustain the measured γ-ray emission.

Unified Astronomy Thesaurus concepts: Solar energetic particles (1491); Solar gamma-ray emission (1497)

1. Introduction

High-energy (>100 MeV) photons in long-duration γ-ray flares (LDGRFs) are known to originate from the decay of pions produced in the interaction of >300 MeV protons and >200 MeV n^{-1} α particles with the solar chromosphere and photosphere (e.g., Vilmer et al. 2011). The LDGRFs are characterized by a delayed and prolonged emission extending up to tens of hours after the impulsive phase (Ryan 2000). Despite the significant progress in recent years as a result of the observations of the Fermi Large Area Telescope (LAT; see Ajello et al. 2021 and references therein), the involved processes are still controversial. Two main competing scenarios have been proposed to explain the acceleration of the interacting particles responsible for the origin of LDGRFs and their subsequent precipitation into the solar atmosphere: (1) particle trapping with/without continuous acceleration within large ($\gtrsim$1 $R_\odot$) coronal loops, characterized by a delayed onset representing the time required by the ions to exceed the pion production threshold energy (Ryan & Lee 1991; Mandzhavidze & Ramaty 1992; Chupp & Ryan 2009; Grechnev et al. 2018; Ryan & de Nolfo 2018; de Nolfo et al. 2019; Ryan et al. 2019; de Nolfo et al. 2021), and (2) coronal mass ejection (CME)-driven shock acceleration, i.e., the dominant mechanism for gradual solar energetic particle (SEP) events measured in situ (Wild et al. 1963; Ramaty et al. 1987; Cliver et al. 1993; Kocharov et al. 2015; Pesce-Rollins et al. 2015; Plotnikov et al. 2017; Gopalswamy et al. 2018a; Jin et al. 2018; Kahler et al. 2018; Kouloumvakos et al. 2020). In the latter case, the high-energy photon emission is also referred to as late-phase γ-ray emission (Share et al. 2018) or sustained γ-ray emission (Kahler et al. 2018). Alternative models predict particle trapping/(re)acceleration in nonflaring closed loops (Hudson 2018) or by electric fields in a current sheet in the wake of a CME (e.g., Akimov et al. 1996; Kocharov et al. 2020).

While LDGRFs tend to be associated with relatively fast CMEs and large SEP events, often with energies typical of ground-level enhancements (GLEs), the apparent connection between these phenomena is questioned by noteworthy counterexamples. For instance, LDGRFs accompanied by CMEs with space speeds as low as 830 km s^{-1} have been reported based on the Coordinated Data Analysis Workshop (CDAW) catalog; in addition, the mean velocity for the sample of 35 LDGRFs listed by de Nolfo et al. (2019) was ~1705 km s^{-1} (~1732 km s^{-1} excluding the two partial-halo CMEs), with 40% of them slower than 1500 km s^{-1}. For comparison, the average speed of the CMEs associated with the 23rd solar cycle GLEs was 2083 km s^{-1} (Gopalswamy et al. 2012). Of particular note is that no CME was observed during the events on 2012 October 23 and November 27, suggesting that a fast and wide CME is not a necessary condition for LDGRFs, although there is evidence for the eruption of magnetic loops and material moving away from the flare region (Share et al. 2018).

On the other hand, the 2012 May 17 GLE event was not linked to one of the larger LDGRFs, and some of the high-energy SEP events measured by the Payload for Antimatter Matter Exploration and Light-nuclei Astrophysics (PAMELA) space experiment were not associated with LDGRFs; analogously, several LDGRFs were accompanied by relatively small SEP events (de Nolfo et al. 2019). Finally, while characterized by one of the longest γ-ray emissions, no significant flux of high-energy SEPs was measured during the 2011 March 7 event; furthermore, the particle release time inferred from L1 observations occurred at least $\sim$10 minutes later than the LDGRF onset (Kahler et al. 2018; Klein et al. 2018).

The possible link between the populations of shock-accelerated ions escaping into interplanetary space and those precipitating onto the solar atmosphere was explicitly investigated by Share et al. (2018) and, more thoroughly, by de Nolfo et al. (2019), who used the high-energy proton observations from PAMELA, the Geostationary Operational Environmental Satellites (GOES), and the twin Solar TErrestrial RElations Observatory (STEREO) spacecraft to reconstruct the spatial distribution of 14 SEP events associated with LDGRFs. The resulting number of $>$500 MeV protons at 1 au ($N_{\rm SEP}$) were compared to the corresponding number of $>$500 MeV protons producing the LDGRFs ($N_{\rm LDGRF}$), as inferred from the Fermi-LAT γ-ray observations by Share et al. (2018). No correlation was found between the $N_{\rm SEP}$ and $N_{\rm LDGRF}$ values, suggesting that the two phenomena are not produced by the same population of CME-driven shock-accelerated ions. Furthermore, the corresponding precipitation fractions $P_N = N_{\rm LDGRF}/(N_{\rm LDGRF} + N_{\rm SEP})$ were found to be characterized by large values, with eight (six) events having $P_N > 10\%$ (20%) and even three events with $P_N > 80\%$, implying that a very large percentage of the overall shock-accelerated particle population would be required to explain the observed LDGRF fluence. These large precipitation fractions are clearly inconsistent with current model predictions, which suggest that SEP back-propagation from the height of the CME-driven shock down to the solar surface is strongly impeded by magnetic mirroring (Hudson 2018; Klein et al. 2018). In fact, only ions injected nearly parallel to the coronal or interplanetary magnetic field lines near the shock in a narrow loss cone can reach a sufficiently dense region of the solar atmosphere to undergo nuclear interactions. Assuming an isotropic particle distribution at the shock, the corresponding fraction amounts to $\sim$1% of the initial population (Klein et al. 2018). Recently, Hutchinson et al. (2022) investigated the mirroring problem extensively using 3D test particle simulations with varying levels of scattering. While strong scattering conditions can occur close to the Sun, back-precipitation was shown to be generally highly inefficient, with instantaneous precipitation fractions lower than 2%. In addition, a strong radial dependence was found for P_N, so that the back-precipitation drastically decreases with increasing injection heights as the CME shock expands. An upper limit on the total precipitation fraction in the CME scenario was evaluated for eight of the 14 events analyzed by de Nolfo et al. (2019) with values ranging from $\sim$0.56% to $\sim$0.93%, increasing with decreasing shock speed (Hutchinson et al. 2022). In fact, faster shocks accelerate particles over larger heliodistances and tend to spend less time close to the solar surface, where the precipitation is more efficient. These modeled precipitation fractions are, on average, almost a factor of $\sim$50 smaller than the values reported by de Nolfo et al. (2019). In addition, the precipitation temporal profiles assessed with the simulations exhibit a much faster decay with respect to experimental observations. Thus, although solar protons are believed to be accelerated to the requisite energy range by CME-driven shocks, their transport in sufficient numbers back to the Sun by means of a robust, repeatable process is a challenge for the widely invoked CME-shock origin model for LDGRFs.

In this work, we critically analyze the assumptions behind the calculation of the $N_{\rm LDGRF}$ and $N_{\rm SEP}$ numbers and further explore the statistical relationship between LDGRFs and SEP events to test the validity of the CME-shock paradigm. The paper is structured as follows. In Section 2, we analyze the uncertainties affecting the comparison between the precipitating and interplanetary proton populations reported by de Nolfo et al. (2019), including the effects of γ-ray flux, SEP events, and interplanetary transport modeling, and discuss the comparison with previous calculations. In Section 3, we investigate the association between LDGRFs and interplanetary type II radio emission that is claimed by Gopalswamy et al. (2018b) to support the CME-shock scenario. Finally, Section 4 summarizes the study and presents our conclusions.

2. Interacting and Interplanetary Protons

2.1. Interacting Protons

Estimates of the number of $>$500 MeV protons producing the observed $>$100 MeV γ-ray emission used in de Nolfo et al. (2019) rely on the work by Share et al. (2018), who carried out a comprehensive analysis of 30 LDGRFs between 2011 and 2015 based on the Fermi-LAT data. These authors used the model by Murphy et al. (1987) to assess the source spatial distribution, accounting for the attenuation effects associated with atmospheric absorption. For instance, their calculation results in $\sim$80% of photons escaping at a heliocentric angle (or central meridian distance) of 70°, with this fraction decreasing to $\sim$47% and $\sim$8% at 85° and 90°, respectively. They also estimated the corresponding hardening in the escaping γ-ray spectrum. In addition, Share et al. (2018) provided a heliocentric angle–dependent correction factor ranging from 1 at the solar limb to $\sim$2.3 at the disk center, accounting for the fact that the ions producing LDGRFs may be characterized by an approximately downward isotropic distribution rather than fully isotropic. However, while flare-accelerated protons are more likely to follow an approximately downward isotropic distribution, this may not be the case for shock-accelerated protons (see Share et al. 2018 and references therein). Therefore, in contrast to de Nolfo et al. (2019), the relative correction factor was not used in this analysis, aiming to provide more conservative lower limits on the precipitation fraction. The $N_{\rm LDGRF}$ numbers from Share et al. (2018) were also compared with those recently estimated by Ajello et al. (2021). The results of the two calculations for the 14 events analyzed by de Nolfo et al. (2019) are reasonably similar with a few exceptions; in particular, according to Ajello et al. (2021), $N_{\rm LDGRF}$ is a factor of $\sim$1.8, $\sim$2.6, and $\sim$1.5 higher for the 2011 June 7, 2011 September 6, and 2012 May 17 events, respectively, while it is about a factor of $\sim$0.4 for the 2014 September 1 event. As discussed below, these differences are reflected in the corresponding precipitation fraction.

Table 1
Relevant Heliographic Coordinates and CME Parameters for the 14 LDGRF-associated SEP Events Analyzed by de Nolfo et al. (2019)

No.	SEP Event	Earth Footpoint	Flare Location	G2014 FR Loc.	DONKI Direction	CDAW Speed
1	2011/03/07	S07W55	N30W48	N32W58	N17W50	2223
2	2011/06/07	N00W55	S21W54	S08W51	S25W52	1321
3	2011/08/04	N05W64	N19W36	N19W30	N14W40	1477
4	2011/08/09	N06W42	N14W69	N08W68	S12W62	1640
5	2011/09/06	N07W57	N14W18	N20W19	N20W20	830
6	2012/01/23	S05W58	N33W21	N30W22	N41W26	2511
7	2012/01/27	S05W47	N33W85	N27W82	N40W75	2541
8	2012/03/07	S07W62	N17E27	N18E31	N30E60	3146
9	2012/05/17	S02W62	N07W88	S07W76	S10W75	1596
10	2012/07/07	N03W53	S13W59	S29W62	S35W65	1907
11	2013/04/11	S05W66	N07E13	N08E11	S07E25	1369
12	2013/10/28	N04W84	S06E28	…	N20E10	1098
13	2014/02/25	S02W48	S12E82	S08E80(b)	S11E78	2153
14	2014/09/01	N02W46	N14E127(a)	N16E117(c)	N01E155	2017

Note.
References. The first two columns report the SEP event number and date, the third column lists the heliographic coordinates of the Earth footpoint, the fourth column gives the location of the parent flares based on the SolarSoft package, the fifth column indicates the CME flux rope location (not available for event 12) estimated by Gopalswamy et al. (2014, G2014), and the sixth column reports the CME direction from the DONKI catalog. Finally, the seventh column lists the CME space speed (km s^{-1}) from the CDAW catalog. (a) Ackermann et al. (2017), (b) Gopalswamy et al. (2015), (c) Gopalswamy et al. (2020).

2.2. Interplanetary Protons

The number of >500 MeV interplanetary protons (N_{SEP}) was estimated by de Nolfo et al. (2019) by combining the multipoint in situ observations from PAMELA/GOES, STEREO-A, and STEREO-B. As comprehensively described in Bruno & Richardson (2021), the SEP spatial distribution on the spherical surface with a 1 au radius was derived by means of a 2D Gaussian model accounting for both longitudinal and latitudinal magnetic connectivity as a function of the spherical distance:

$$\delta = \arccos[\sin(\theta)\sin(\theta_{sep}) + \cos(\theta)\cos(\theta_{sep})\cos(\phi - \phi_{sep})], \quad (1)$$

where θ and ϕ are the Stonyhurst heliographic latitude and longitude (e.g., of the observing spacecraft footpoint), and (θ_{sep}, ϕ_{sep}) are the coordinates of the distribution peak (main SEP propagation axis). The distribution standard deviation assumes a spherical symmetry, so that $\sigma^{\theta} = \sigma^{\phi} = \sigma$. The longitude of the SEP propagation axis (ϕ_{sep}) was obtained by the best fit of the three spacecraft intensities, while its latitudinal angle θ_{sep} is not derivable from experimental data.

The flare locations and CME directions/space speeds of the 14 events analyzed by de Nolfo et al. (2019) are reported in Table 1. The first two columns list the event numbers and dates. The footpoint locations of the magnetic field line passing through the Earth, mapped ballistically back to 2.5 $R_{\odot}$ (Bruno & Richardson 2021), are shown in the third column. The fourth column gives the flare coordinates from the SolarSoft package. The next two columns refer to the CME directions from Gopalswamy et al. (2014), who fitted a flux rope to the CMEs in the SOlar and Heliospheric Observatory (SOHO) and STEREO images using the graduated cylindrical shell (GCS) model (Thernisien 2011), and from the Space Weather Database Of Notifications, Knowledge, Information (DONKI) catalog, based on the geometric triangulation of SOHO and STEREO coronagraph measurements. Finally, the CME space speeds from the CDAW catalog, relying on a cone model correction of sky plane speeds (Gopalswamy et al. 2010), are reported in the last column. In general, accounting for the associated uncertainties, the heliographic coordinates of the flares and CMEs are relatively similar, while a large deviation suggests a significant nonradial motion component or that the flare location is not directly under the center of the CME. On the other hand, there is a remarkable (up to tens of degrees) discrepancy between the CME latitudinal angles in Table 1. Indeed, it is well known that current CME catalogs using different analysis methods and instruments generally disagree on the properties (speed, width, and direction) of individual CMEs associated with SEP events (Richardson et al. 2015). However, CME reconstructions based on multiple viewpoints typically have smaller errors (see, e.g., Verbeke et al. 2022). For instance, the uncertainties on the CME latitudinal/longitudinal angles in the DONKI catalog are typically 5°/10° and 15°/30° for parameter estimates based on three- and one-spacecraft observations, respectively; a similar trend characterizes the errors on the CME speeds/widths (L. Mays, private communication, 2020).

To avoid the uncertainties related to the choice of a particular CME catalog, de Nolfo et al. (2019) used the latitude of the parent flares. To assess the effect of such approximation, we recalculated the N_{SEP} values by using the flare locations, as well as the CME directions from DONKI and Gopalswamy et al. (2014). In addition, the connection angles δ (Equation (1)) relative to each spacecraft location were evaluated using the corresponding Parker spiral magnetic field line footpoints at 2.5 $R_{\odot}$, which is similar to the typical particle release height inferred for GLE events assuming that the particles are accelerated at CME-driven shocks (Reames 2009; Gopalswamy et al. 2013), while they were computed at 30 $R_{\odot}$ in de Nolfo et al. (2019). Consequently, the new N_{SEP} values also account for the relatively small differences associated with the footpoint calculation.

The number of >500 MeV interplanetary protons N_{SEP} was derived by de Nolfo et al. (2019) using the >80 MeV proton

spatial distributions as proxies of those of >500 MeV protons, which are not directly measurable. In fact, the STEREO proton observations are limited to 100 MeV, and an estimate based on the extrapolation of the spectral fits above 500 MeV is unreliable due to the large associated uncertainties. For this reason, de Nolfo et al. (2019) considered the obtained $N_{\rm SEP}$ values as upper limits. However, this assumption is strictly valid only for well-connected SEP events, while the proton numbers could be larger, especially for events with poorer connectivity, if characterized by a narrow spatial distribution. In order to compute more conservative $N_{\rm SEP}$ upper limits that take into account the different widths of the spatial distributions at higher energies, we developed the following approach.

1. The >80 MeV differential energy spectrum at the shock nose was assumed to be described by an Ellison & Ramaty (1985) functional form: $I_n(E) \propto E^{-\alpha_n}\exp(-E/E_0)$. The spectrum of the 2012 May 17 GLE measured by PAMELA, with parameters α_n ~2.4 and E_0 ~500 MeV (Bruno et al. 2018), was used as a proxy of the spectrum at the shock nose.
2. The $E > E_t$ energy-integrated intensities at the shock nose ($J_n^{E_t} = \int_{E_t}^{\infty} I_n(E)dE$) and at a given spacecraft spherical distance δ_{E_t} ($J_\delta^{E_t} = \int_{E_t}^{\infty} I_\delta(E)dE$) are related by $J_\delta^{E_t} = J_n^{E_t} C_\delta^{E_t}$, with the angular correction factor given by

$$C_\delta^{E_t} = \exp\left[-\frac{1}{2}\left(\frac{\delta_{E_t}}{\sigma_{E_t}}\right)^2\right], \quad (2)$$

   where the Gaussian standard deviation σ_{E_t} describes the width of the corresponding SEP spatial distribution.
3. The connection angle δ_{E_t} is energy-dependent; in fact, the peak of the spatial distribution, on average located on field lines with footpoints westward of the source coordinates, tends to move eastward with increasing energy (Bruno & Richardson 2021). The SEP peak longitudinal displacement can be parameterized as

$$\phi_{\rm sep}(E) - \phi_s = \phi_0 - \phi_1 \log(E), \quad (3)$$

   where ϕ_s is the longitude of the parent flare/CME. For this analysis, we set ϕ_1 to 4.81, i.e., the mean value obtained by Bruno & Richardson (2021) using a sample of 32 SEP events, while ϕ_0 was computed event by event based on the longitudinal deviation obtained for the >80 MeV spatial distribution.
4. The >80 and >500 MeV energy-integrated intensities at the spherical distance δ associated with the Earth footpoint, J_δ^{80} and J_δ^{500}, were obtained from de Nolfo et al. (2019), while the ratio of the corresponding energy-integrated spectra at the shock nose, $R_J = J_n^{500}/J_n^{80}$, was derived based on the α_n and E_0 parameters.
5. Then, the >500 MeV energy-integrated spectrum at the shock nose was calculated as

$$J_n^{500} = J_\delta^{500}/C_\delta^{500} = R_J\, J_n^{80} = R_J\, J_\delta^{80}/C_\delta^{80}, \quad (4)$$

   where C_δ^{80} is the angular correction factor based on the σ_{80} value computed by de Nolfo et al. (2019) for each of the 14 SEP events.
6. The corresponding standard deviation was evaluated as

$$\sigma_{500} = \sqrt{-\frac{1}{2}\frac{(\delta_{500})^2}{\log(C_\delta^{500})}}, \quad (5)$$

   with δ_{500} derived from Equation (3)—implying an ~8°.8 average displacement of the distribution peak from 80 to 500 MeV—and this value was used in place of σ_{80} in the calculation by de Nolfo et al. (2019) to estimate the number of interplanetary protons above 500 MeV.

We note that all of the used quantities—in particular, the individual σ_{80} values—are based on experimental data. The only assumptions relate to the ϕ_1 value and the shock nose spectrum, which, however, was approximated by the hardest SEP spectrum available with >500 MeV proton data observed by PAMELA in solar cycle 24. The calculated σ_{500} standard deviations range from ~17% to ~92% of the corresponding σ_{80} values.

Special attention was given to those SEP events with no appreciable intensities or with a significant background from a previous eruption at a given spacecraft location in order to derive conservatively high upper limits on the corresponding $N_{\rm SEP}$ numbers. In particular, for the 2011 August 9 and 2012 July 7 events, with no relevant SEP signal at STEREO-B, we assessed the >80 MeV spatial distribution based on near-Earth and STEREO-A measurements by evaluating the peak longitude with Equation (3) using the mean ϕ_0/ϕ_1 values from Bruno & Richardson (2021) to constrain the fit. The same method was applied to the longitudinally well-connected event on 2011 June 7, characterized by a large background at both STEREOs, for which we assumed a 20° standard deviation at 80 MeV, in contrast to the ~40° value used by de Nolfo et al. (2019). Finally, for the STEREO-B observations relative to the events on 2011 March 7, 2012 January 27, and 2013 October 10, which were significantly influenced by ongoing events, we conservatively assumed that the effective background-subtracted intensities were a factor of 3 lower than assumed by de Nolfo et al. (2019).

2.3. Results

The calculated $N_{\rm LDGRF}$ and $N_{\rm SEP}$ numbers are summarized in Table 2, while the corresponding scatter plots are shown in Figure 1; the three panels correspond to the upper limits on the $N_{\rm SEP}$ numbers computed using the flare locations (blue) and the CME directions from Gopalswamy et al. (2014; green) and DONKI (red) reported in Table 1. As discussed in Section 2.1, the $N_{\rm LDGRF}$ values used do not account for the heliocentric angle–dependent correction factor for a downward isotropic distribution, in contrast to de Nolfo et al. (2019). The corresponding Kendall (τ) and Spearman (R_s) rank correlation coefficients are reported in each panel along with the relative p-values. Similar to de Nolfo et al. (2019), we did not consider the Pearson coefficient, since it is greatly affected by outliers and the distribution points are not uniformly distributed. The correlation is in no case statistically significant, as suggested by the corresponding p-values, which are higher than the typical threshold of 0.05 for the rejection of the null hypothesis (no correlation). However, for the case of the Gopalswamy et al. (2014) latitudes, the associated probability is 11% and 14%, respectively, for the Kendall and Spearman coefficients, suggesting a certain trend toward significance, although the results cannot be considered conclusive. In general, the

Table 2
Summary of Estimated Proton Numbers

No. (1)	SEP Event (2)	N_{LDGRF} S2018 (3)	N_{LDGRF} A2021 (4)	Flare N_{SEP} (5)	Flare P_N^{S2018} (6)	Flare P_N^{A2021} (7)	G2014 N_{SEP} (8)	G2014 P_N^{S2018} (9)	G2014 P_N^{A2021} (10)	DONKI N_{SEP} (11)	DONKI P_N^{S2018} (12)	DONKI P_N^{A2021} (13)
1	2011/03/07	7.20×10^{28}	6.44×10^{28}	1.42×10^{29}	33.67	31.23	1.63×10^{29}	30.70	28.38	6.54×10^{28}	52.42	49.63
2	2011/06/07	1.10×10^{28}	1.95×10^{28}	1.35×10^{29}	7.55	12.64	1.43×10^{28}	43.47	57.69	2.05×10^{29}	5.09	8.68
3	2011/08/04	1.20×10^{28}	9.00×10^{27}	3.69×10^{28}	24.56	19.63	3.69×10^{28}	24.56	19.63	3.13×10^{28}	27.69	22.31
4	2011/08/09	4.00×10^{27}	2.70×10^{27}	1.47×10^{30}	0.27	0.18	6.36×10^{29}	0.62	0.42	1.32×10^{29}	2.94	2.01
5	2011/09/06	2.20×10^{28}	5.80×10^{28}	7.39×10^{28}	22.95	43.99	7.83×10^{28}	21.94	42.56	7.83×10^{28}	21.94	42.56
6	2012/01/23	3.00×10^{28}	2.47×10^{28}	1.27×10^{29}	19.11	16.28	1.03×10^{29}	22.57	19.35	2.27×10^{29}	11.69	9.83
7	2012/01/27	1.70×10^{28}	1.72×10^{28}	2.17×10^{30}	0.78	0.79	1.39×10^{30}	1.21	1.22	3.87×10^{30}	0.44	0.44
8	2012/03/07	1.73×10^{30}	1.86×10^{30}	8.67×10^{31}	1.96	2.10	8.67×10^{31}	1.96	2.10	9.84×10^{31}	1.73	1.85
9	2012/05/17	1.50×10^{27}	2.29×10^{27}	1.10×10^{30}	0.14	0.21	1.14×10^{30}	0.13	0.20	1.02×10^{30}	0.15	0.22
10	2012/07/07	9.00×10^{27}	7.50×10^{27}	6.80×10^{27}	56.95	52.44	3.12×10^{28}	22.38	19.38	6.18×10^{28}	12.71	10.82
11	2013/04/11	7.40×10^{27}	6.00×10^{27}	3.58×10^{29}	2.03	1.65	3.63×10^{29}	2.00	1.62	3.21×10^{29}	2.25	1.84
12	2013/10/28	4.00×10^{26}	⋯	1.41×10^{30}	0.03	⋯	1.37×10^{30}	0.03	⋯	1.43×10^{30}	0.03	⋯
13	2014/02/25	8.80×10^{29}	7.19×10^{29}	1.05×10^{32}	0.83	0.68	9.83×10^{31}	0.89	0.73	1.03×10^{32}	0.84	0.69
14	2014/09/01	1.99×10^{30}	7.40×10^{29}	5.68×10^{32}	0.35	0.13	5.66×10^{32}	0.35	0.13	6.00×10^{32}	0.33	0.12

Note. Columns (1) and (2) report the SEP event number and date; columns (3) and (4) list the number of >500 MeV interacting protons (N_{LDGRF}) according to Share et al. (2018, S2018) and Ajello et al. (2021, A2021); and columns (5)–(7), (8)–(10), and (11)–(13) report the number of >500 MeV interplanetary protons (N_{SEP}) and the corresponding precipitation fractions (P_N, %) using the calculations of N_{SEP} using latitudes of the associated flare or CME latitudes from Gopalswamy et al. (2014, G2014) and the DONKI catalog (see Table 1).

correlation appears to be essentially controlled by the three points in the top right corner of the panels (events on 2012 March 7, 2014 February 25, and 2014 September 1), since the rest of the sample does not seem to follow any specific trend ($\tau = -0.07$, $p = 0.79$; $R_s = -0.14$, $p = 0.70$). We also note that the results do not include the outlying point (black circle) for the 2013 October 28 event, since the origin of the associated γ-ray emission is uncertain (Share et al. 2018); in addition, this event is not included in the Gopalswamy et al. (2014) calculation (see Table 1). Finally, the corresponding bi-logarithmic regression lines are also shown in Figure 1, emphasizing that the average N_{LDGRF}/N_{SEP} ratio is not constant but decreases with increasing N_{SEP} values.

The corresponding lower limits on the precipitation fractions are displayed in the top panel of Figure 2 and reported in Table 2. We note that, despite the conservative assumptions described in the previous sections, the precipitation fraction is still higher than 10%–20% for five or six of the 14 analyzed events, depending on the latitudes used. Interestingly, no particular trend with CME- or flare-related parameters was found for the P_N distribution; in particular, low-/high-fraction occurrences appear to be independent of the CME speed. On the other hand, it has been shown by Hutchinson et al. (2022) that smaller precipitation fractions tend to occur for longer-duration events associated with faster CMEs. In contrast, a relatively high P_N value was obtained for the 2011 March 7 and 2012 January 23 events, both accompanied by long-duration γ-ray emission and fast CMEs (2223 and 2511 km s^{-1}), while a low precipitation fraction was found for the short-duration event on 2013 April 11 linked to a 1369 km s^{-1} CME.

As mentioned in Section 2.1, we compared the N_{LDGRF} numbers from Share et al. (2018) to the ones derived by Ajello et al. (2021) and found a reasonable agreement for most events. The results in terms of precipitation fractions are displayed in the bottom panel of Figure 2, where for the upper limits on the N_{SEP} numbers we used the estimates made with the latitudes from Gopalswamy et al. (2014). These were assumed to be the most reliable because the CME direction is likely a better approximation of the SEP propagation axis, and the CME parameters in the DONKI catalog are often based on real-time calculations. As aforementioned, the largest variations involve the eruptions on 2011 June 7 and 2011 September 6, for which the N_{LDGRF} from Ajello et al. (2021) are a factor of ~1.8 and ~2.6 higher, respectively. We note that, for both calculations, P_N is greater than 20% for six events.

2.4. Comparison with Other Calculations

The comparison with the previous work by de Nolfo et al. (2019) is shown in Figure 3. It can be noted that the precipitation fractions we obtained are often significantly lower, as a consequence of the removal of the heliocentric angle–dependent correction factor on the N_{LDGRF} numbers, as well as the improved estimate of the SEP distributions above 500 MeV described in the previous section. However, even accounting for these more conservative assumptions, we confirm the conclusions of de Nolfo et al. (2019) about the lack of a statistically significant correlation between the number of SEP protons and the number of protons required to account for the γ-ray emission. Furthermore, a high precipitation fraction is required for several of the events that appears inconsistent with a CME-shock origin of LDGRFs. Figure 3 also includes results from Gopalswamy et al. (2021), who modified the proton numbers from de Nolfo et al. (2019) with additional correction factors, resulting in a high statistical correlation between N_{LDGRF} and N_{SEP}. Specifically, they increased the N_{LDGRF} values for eruptions near and behind the limb, assuming an underestimate for the atmospheric attenuation of the γ-ray flux. In particular, they computed a correction factor of 560 for the 2014 September 1 event. Since this event occurred behind the limb, it cannot be excluded that the flux computed by Share et al. (2018; and Ajello et al. 2021) was somewhat underestimated. On the other hand, as LDGRFs are highly extended, we would not expect the reconstructed γ-ray flux to account for only ~0.18% (i.e., 1/560) of the total emitted flux. This large correction factor also increases the

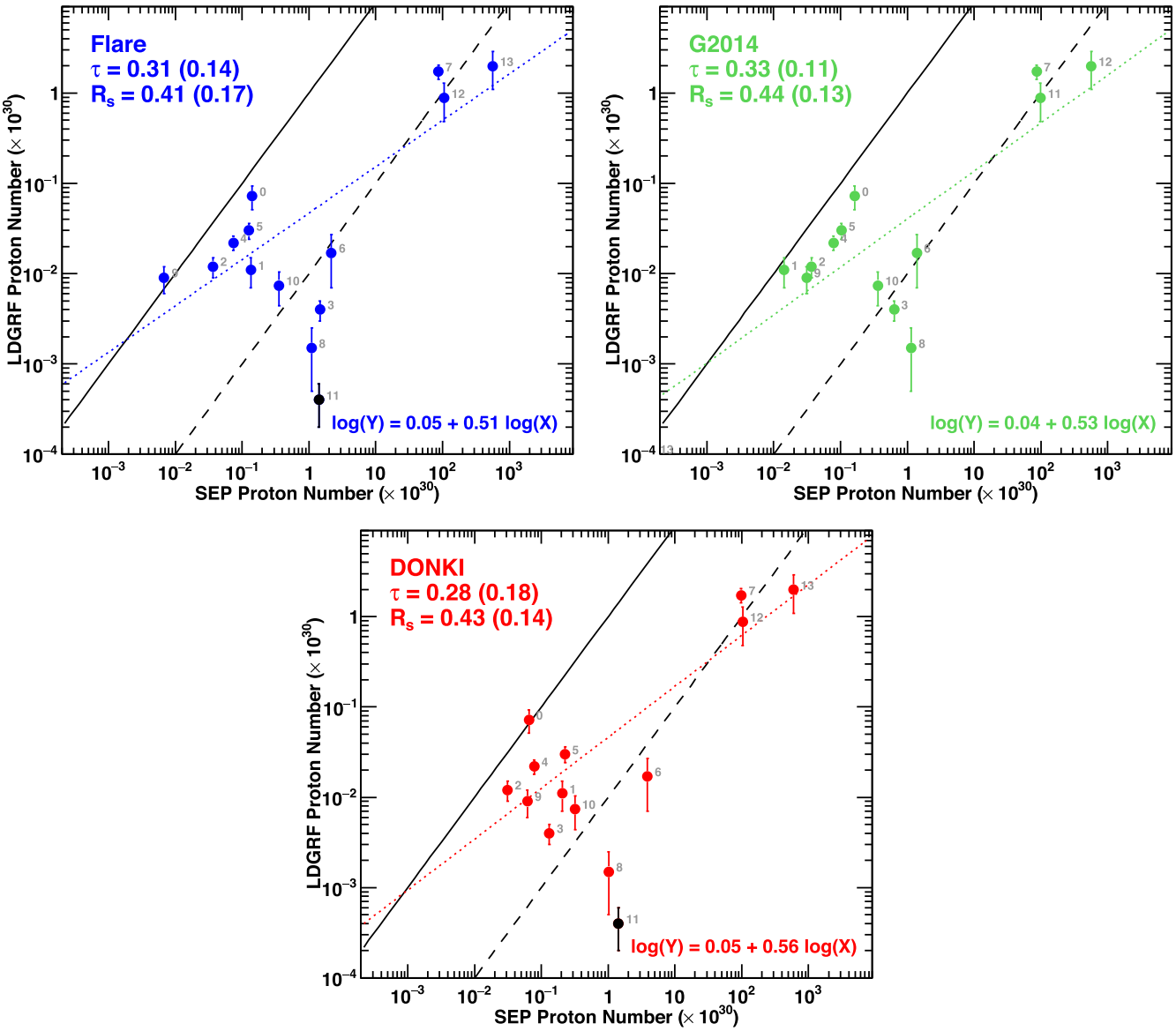

Figure 1. Scatter plots of the $N_{\rm LDGRF}$ vs. $N_{\rm SEP}$ values obtained by using the upper limits on the number of >500 MeV interplanetary protons. The three panels report the calculations made implementing the flare latitudes (blue; top left panel) and the CME latitudinal angles from Gopalswamy et al. (2014, G2014; green, top right panel) and DONKI (red; bottom panel) – see Table 1, with the corresponding Kendall (τ) and Spearman (R_s) correlation factors and relative p-values between brackets. The event numbers from Table 1 are given adjacent to the data points. The colored dotted lines indicate the corresponding bi-logarithmic regression lines, with parameters reported in the bottom right corner. The solid and dashed black lines mark the 1-to-1 and 1-to-100 correspondences, respectively. The black circle marks the 2013 October 28 event, which is not included in the correlation and the regression estimates.

precipitation factor by approximately 2 orders of magnitude, to ∼82%, which cannot be reconciled with the predictions of current models of particle precipitation from a CME shock (Hutchinson et al. 2022). Furthermore, we note that the γ-ray occultation was already accounted for by Share et al. (2018), so the final $N_{\rm LDGRF}$ numbers of Gopalswamy et al. (2021) are actually based on an overcorrection for this effect.

Analogously, Gopalswamy et al. (2021) overcounted the SEP latitudinal correction factor already implemented by de Nolfo et al. (2019) when calculating $N_{\rm SEP}$. In addition, their correction method relies on some questionable assumptions. In particular, for the shock nose, they assumed a simple inverse power-law energy spectrum with index $\alpha_n = 2$ extending to infinite energies. However, this is inconsistent with historical neutron monitor observations that show a $\geqslant 3$ index even during the initial phase of major GLEs (e.g., Vashenyuk et al. 2011; Mishev et al. 2012; Koldobskiy et al. 2022; Mishev 2023). Indeed, their spectral fit studies are based on the analysis of the GOES proton intensities at low energies (10–100 MeV); furthermore, the large uncertainties associated with the GOES uncalibrated energy channels typically result in systematically harder spectra (Bruno 2017). We also note that their energy-dependent width calculation was only applied to five eruptions with high latitudinal angles. On the other hand, given the spherical symmetry assumed for the SEP spatial distribution, the decrease of the associated standard deviation with increasing energy affects both the SEP longitudinal and latitudinal extent. In fact, we found that correcting the whole event sample with the same criterion results in a systematic shift of the $N_{\rm SEP}$ numbers toward higher values (including the events with the largest $N_{\rm SEP}/N_{\rm LDGRF}$ ratios) and in a remarkably lower correlation with the $N_{\rm LDGRF}$ numbers. Finally, Gopalswamy et al. (2021)

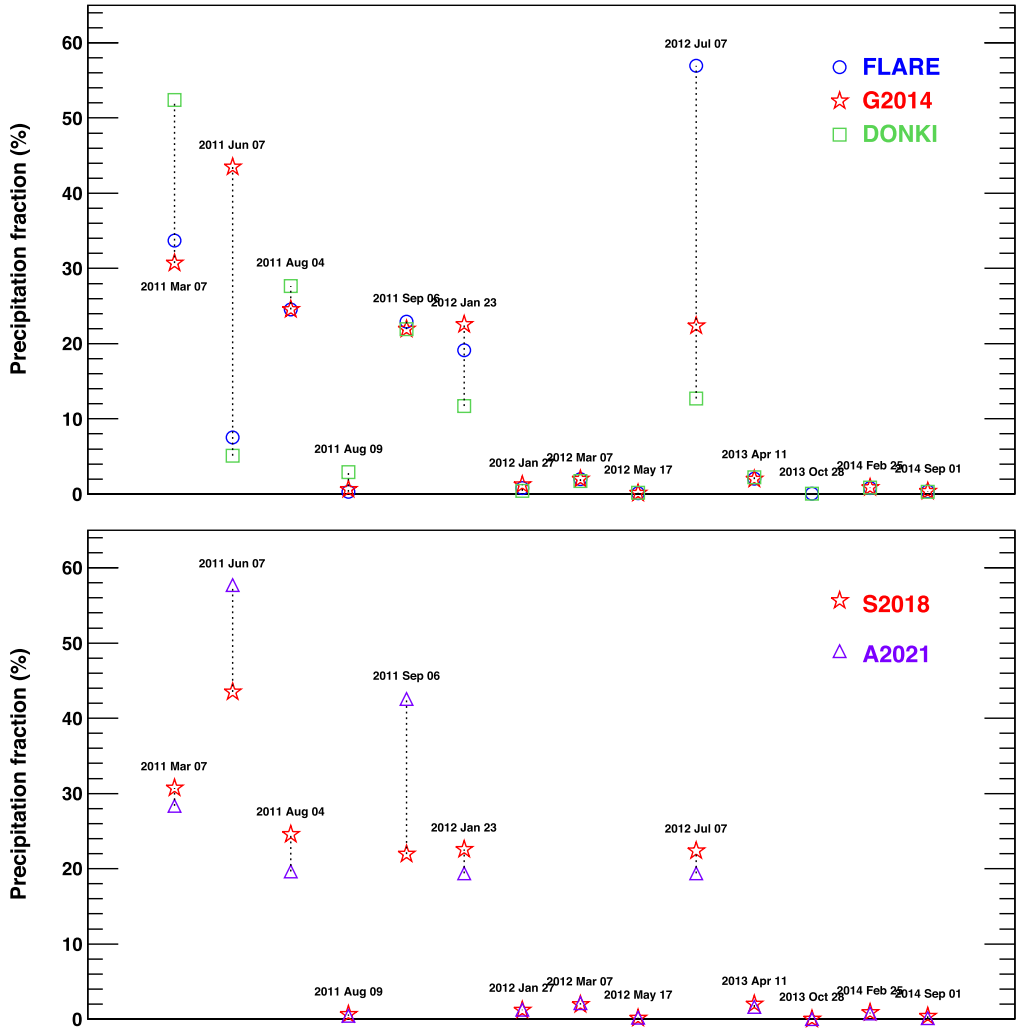

Figure 2. Top: lower limits on the precipitation fractions $P_N = N_{\rm LDGRF}/(N_{\rm LDGRF} + N_{\rm SEP})$ relative to the proton numbers assuming the different latitudinal angles displayed in Figure 1. Bottom: comparison between the precipitation fraction lower limits using the $N_{\rm LDGRF}$ values from Share et al. (2018; red) and Ajello et al. (2021, A2021; green) and the upper limits on the $N_{\rm SEP}$ numbers derived using the Gopalswamy et al. (2014, G2014) latitudes. The dotted lines are to guide the eye.

approximated the CME latitudes with the corresponding plane-of-the-sky position angles from the CDAW catalog affected by projection effects resulting in systematic errors in the CME direction. For instance, the position angles evaluated for the 2012 January 23 and 2012 March 7 CMEs are N56 and N33, respectively, compared to the N30 and N18 CME latitudes computed by Gopalswamy et al. (2014) with multi-spacecraft observations using the GCS method. Thus, for these reasons, we question the validity of the high correlation between the "corrected" values of $N_{\rm SEP}$ and $N_{\rm LDGRF}$ claimed by Gopalswamy et al. (2021).

2.5. Interplanetary Transport Effects

De Nolfo et al. (2019) accounted for some of the interplanetary transport effects on high-energy protons, in particular the multiple crossings experienced by particles at 1 au due to local scattering that increase the apparent SEP intensity, by means of 3D test particle simulations including the effects of the heliospheric current sheet (HCS). In particular, they conservatively assumed a mean free path $\lambda = 0.5$ au. This value corresponds to an average number of 1 au crossings of 8 and 11 for periods of solar magnetic polarity A^+ and A^-, respectively (see their Table 4). Consequently, the calculated $N_{\rm SEP}$ values—corrected by the corresponding number of 1 au crossings—are expected to be overestimated and the P_N values therefore underestimated under more turbulent conditions. We note that a smaller mean free path of 0.3 au was evaluated for the 2012 May 17 event using PAMELA measurements (de Nolfo et al. 2019; Dalla et al. 2020). Considering an even smaller mean free path of 0.1 au, the numbers of 1 au crossings computed by de Nolfo et al. (2019) are 21 and 30, respectively, for A^+ and A^- polarity, so the resulting $N_{\rm SEP}$ numbers would be 62%–63% smaller. While these estimates do not affect the level of correlation with the $N_{\rm LDGRF}$ numbers, since the intensity is changed by a similar factor for all events, they have noteworthy influences on the corresponding precipitation fractions. Figure 4 demonstrates the effect of using a higher level of scattering in the estimate of the number of crossings. It can be seen that the fractions are considerably higher for $\lambda = 0.1$ au, with an ∼40% minimum value for six events. We note that these values would be even higher using the $N_{\rm LDGRF}$ values from Ajello et al. (2021) or the flare/DONKI latitudes in the $N_{\rm SEP}$ calculation.

There are also uncertainties in modeling the SEP spatial distribution, assumed to be described by a 2D Gaussian given the limited number of observation points (typically three or

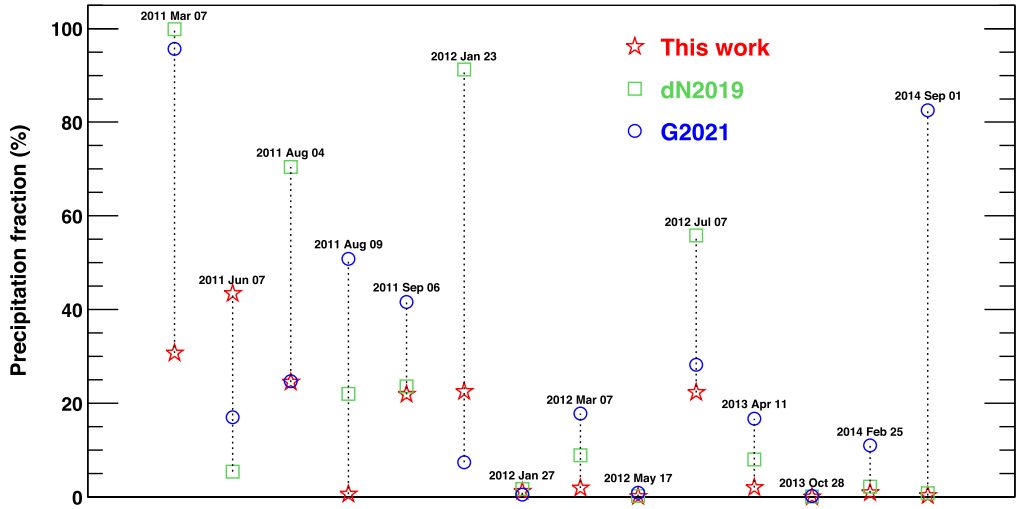

Figure 3. Comparison between the precipitation fraction lower limits derived in this work using the N_{SEP} upper limits based on the CME latitudes from Gopalswamy et al. (2014) and the precipitation fractions estimated by de Nolfo et al. (2019, dN2019) and Gopalswamy et al. (2021, G2021). All of the calculations rely on the N_{LDGRF} values from Share et al. (2018). The dotted lines are to guide the eye.

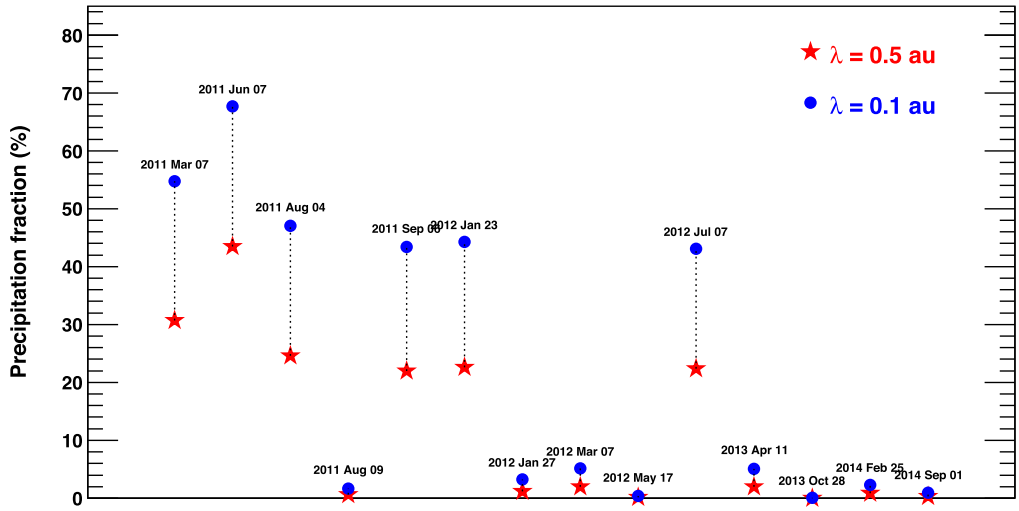

Figure 4. Comparison between the precipitation fraction lower limits using the different interplanetary turbulence conditions as parameterized by the mean free path λ. Both calculations are based on the N_{SEP} upper limits obtained with the CME latitudes from Gopalswamy et al. (2014) and the N_{LDGRF} values from Share et al. (2018).

less). It is likely that the "true" distribution may substantially deviate from a Gaussian, and, in particular, it may include longitudinal and latitudinal asymmetries, for example, related to solar wind structures (e.g., Lario et al. 2022). In addition, the propagation of high-energy SEPs has been shown to be strongly influenced by the HCS and drifts associated with the gradient and curvature of the Parker spiral magnetic field, with significant differences between epochs of A^+ and A^- polarities (Dalla et al. 2020). Furthermore, it was found that SEP events with a source region closer to the HCS ($<10°$) were more likely to be associated with GLE events (Waterfall et al. 2022).

3. LDGRFs and Type II Radio Emission

Possible support for the CME-shock origin of LDGRF events comes from the correlation between LDGRF durations and the ending frequencies and durations of the interplanetary type II bursts associated with the CMEs accompanying the γ-ray emission reported by Gopalswamy et al. (2018a), since this radio emission is indicative of particle acceleration occurring at a shock. More extended shock acceleration, as indicated by the duration of the emission and its ending frequency (lower frequencies correspond to larger distances from the Sun), might be expected to lead to longer-duration particle precipitation and LDGRFs. To gain further insight into the interpretation of this result and its significance, we compared the γ-ray event parameters used by Gopalswamy et al. (2018a) with those obtained with three independent estimates by Share et al. (2018), Winter et al. (2018), and Ajello et al. (2021). In the case of the data set by Ajello et al. (2021), only the LDGRF durations were provided (see their Table 1). Several important differences can be pointed out. We first note that, unlike Share et al. (2018) and Winter et al. (2018), who analyzed 33 and 29 LDGRFs, respectively, Gopalswamy et al. (2018a) only considered the subsample of the 13 largest γ-ray events with durations exceeding ∼5 hr. The minimum duration requirement was justified by the the need to avoid any association with impulsive-flare emission. Subsequently, Gopalswamy et al. (2019) reported that the relationship between γ-ray emission times and type II end frequencies and durations also holds after

Table 3
Onset Times (hh:mm) and Durations (hr) for the LDGRF Events Analyzed by Gopalswamy et al. (2019, G2019), Share et al. (2018, S2018), Winter et al. (2018, W2018), and Ajello et al. (2021, A2021)

No.	Date	G2019		S2018		W2018		A2021
		T_{start}	ΔT	T_{start}	ΔT	T_{start}	ΔT	ΔT
1	2011/03/07	20:12	21.02	20:00	15.00	20:15	10.10	15.80
2	2011/06/02	07:46	6.98	08:10	3.83	09:43	0.70	…
3	2011/06/07	06:41	3.08	07:00	3.00	07:34	0.90	6.00
4	2011/08/04	…	…	04:10	3.00	04:59	0.60	2.30
5	2011/08/09	…	…	08:03	0.05	…	…	0.87
6	2011/09/06	…	…	22:21	0.98	22:13	0.60	2.00
7	2011/09/07	…	…	22:45	2.42	23:36	1.00	2.02
8	2011/09/24	…	…	09:40	0.07	…	…	1.20
9	2012/01/23	03:59	15.43	04:20	7.67	04:07	5.20	5.90
10	2012/01/27	18:37	3.59	19:00	3.00	19:44	1.90	6.80
11	2012/03/05	04:09	4.25	04:30	5.50	04:12	3.60	4.40
12	2012/03/07	00:24	20.47	00:28	19.55	00:45	19.50	20.30
13	2012/03/09	03:53	8.85	04:30	6.00	05:16	3.80	7.20
14	2012/03/10	17:44	11.62	20:00	6.00	…	…	6.00
15	2012/05/17	01:47	3.08	02:10	3.17	02:17	1.90	2.60
16	2012/06/03	…	…	17:54	1.10	17:39	0.40	1.90
17	2012/07/06	…	…	23:14	1.77	23:18	0.90	1.27
18	2012/10/23	…	…	03:20	2.00	…	…	1.90
19	2012/11/27	…	…	15:55	0.27	15:49	0.80	0.17
20	2013/04/11	…	…	07:10	0.33	07:01	0.60	0.38
21	2013/05/13	02:17	7.47	02:30	3.50	04:32	0.70	4.00
22	2013/05/13	16:05	8.69	17:00	6.00	17:17	3.80	6.10
23	2013/05/14	01:11	5.99	01:20	5.67	01:12	5.40	5.90
24	2013/05/15	01:48	3.61	02:00	7.00	…	…	3.50
25	2013/10/11	…	…	07:14	0.27	06:32	1.10	0.38
26	2013/10/25	…	…	08:02	1.47	08:20	0.60	1.40
27	2013/10/28	…	…	15:20	1.67	15:34	1.20	1.60
28	2014/01/06	…	…	…	…	07:25	1.10	0.27
29	2014/01/07	…	…	…	…	18:42	0.80	1.05
30	2014/02/25	00:49	8.46	00:50	4.67	01:11	6.60	8.40
31	2014/09/01	11:11	3.92	11:02	4.83	11:02	1.90	2.50
32	2014/09/10	…	…	…	…	17:47	0.60	0.30
33	2015/06/21	02:36	14.06	02:20	11.67	05:24	0.50	11.50
34	2015/06/25	…	…	…	…	09:25	0.70	2.40
35	2017/09/06	12:02	18.43	…	…	…	…	13.33
36	2017/09/10	16:06	15.18	…	…	…	…	13.90

Note. The dots (…) indicate events not included in the calculation.

the inclusion of events with a >3 hr duration. The temporal information about the interplanetary radio data is based on the Wind/WAVES type II burst catalog, with refined emission ending times.

Another important difference concerns the estimation of the event start T^{start} and stop T^{stop} times with the Fermi-LAT data. Gopalswamy et al. (2019) took T^{start} as the GOES soft X-ray peak time "to avoid the impulsive phase," while T^{stop} was obtained as the mid-time between the last data point above the background and the next data point based on the Fermi-LAT "light-bucket" time profiles also used by Share et al. (2018). However, as reported in Table 3 and demonstrated in Figure 5, their start and even end times are significantly different from those evaluated by Share et al. (2018), who, in particular, fit the onset phase based on higher-resolution (4 minute) LAT data, extrapolating to the background level. Similar discrepancies are obtained with the values by Winter et al. (2018), which are based on the maximum-likelihood method used by the LAT team. The Ajello et al. (2021) results are not included in Figure 5, since they did not provide the onset times; however, their event durations are closest to those estimated by Share et al. (2018). Gopalswamy et al. (2019) estimated T^{start} values that occur, on average, for the sample of events in common ∼21.2 and ∼51.6 minutes earlier with respect to the calculations by Share et al. (2018) and Winter et al. (2018). In some cases, the differences are larger than 2 hr. In addition, their T^{stop} values are typically later with respect to those from the same authors. As a result, the event durations calculated by Gopalswamy et al. (2019) are, on average, ∼2.0 and ∼4.6 hr longer with respect to those computed by Share et al. (2018) and Winter et al. (2018), respectively. The discrepancy is notable for some events. As an example, the durations estimated by Gopalswamy et al. (2019) for the 2011 March 7 and 2012 January 23 events are ∼5–11 and ∼8–10 hr longer, respectively, bringing them substantially closer to the durations of the corresponding interplanetary type II bursts. However, as demonstrated by the right panel in Figure 5, a significant discrepancy also exists between the Share et al. (2018) and

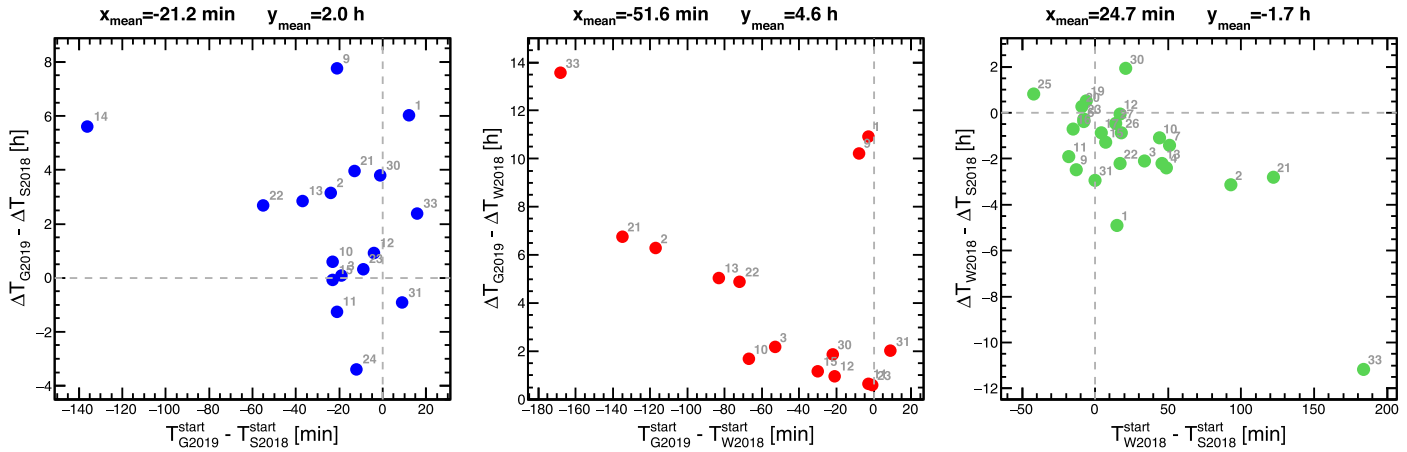

Figure 5. Scatter plots of the difference between the γ-ray event durations ΔT vs. the difference between the corresponding onset times $T^{\rm start}$, based on the estimates from Gopalswamy et al. (2019, G2019), Share et al. (2018, S2018), and Winter et al. (2018, W2018). The event numbers in Table 3 are given adjacent to the data points.

Winter et al. (2018) values, highlighting the large uncertainties characterizing the estimates of the LDGRF times as a result of the Fermi-LAT limited time resolution and duty cycle.

An interesting aspect is the onset time of the 2011 March 7 LDGRF. We note that, even using the most delayed $T_{\rm start}$ value computed by Winter et al. (2018; 20:15 UT), the associated emission commenced ∼11 and ∼10 minutes earlier than the solar particle release times[6] computed with the velocity dispersion analysis by Klein et al. (2018) and Xie et al. (2016), respectively, which is inconsistent with a CME-shock origin. Furthermore, the 20:20 UT LDGRF onset time of Share et al. (2018) and the later release time derived by other authors (e.g., 20:37 UT according to Paassilta et al. 2017) make the CME association even more unlikely. Similar conclusions were also drawn by Kahler et al. (2018).

The implications of using different estimates of LDGRF duration in terms of correlation between the γ-ray and radio emissions are demonstrated in Figure 6. The left and right panels show the scatter plots of the γ-ray durations versus type II end frequencies and durations, respectively. The top panels display the original comparison by Gopalswamy et al. (2019), while the other three rows report the corresponding plots obtained by using the LDGRF durations of Share et al. (2018), Winter et al. (2018), and Ajello et al. (2021). The number of events used (listed in the panels) is larger for the last three samples, accounting for events with durations of <3 hr. In each panel, the radio parameters are taken from Gopalswamy et al. (2019); for the events not present in Gopalswamy et al. (2019), we referred to the radio data from the Wind/WAVES type II burst catalog. The open points mark the event subsample not included by Gopalswamy et al. (2019). As shown by the Kendall and Spearman coefficients at the top of the panels, the anticorrelation between the LDGRF duration and the type II ending frequency and the correlation between the LDGRF and the type II durations are significant using the Gopalswamy et al. (2019) data, as reported in that paper. However, the level of correlation drastically decreases when using the other three estimates of the LDGRF duration, even using the Pearson coefficient, which is more sensitive to outliers and not used in this analysis. As discussed above, the durations of a few LDGRF events (e.g., 2012 March 7 and 2012 January 23) were substantially overestimated by Gopalswamy et al. (2019) compared to the other studies, and the scatter plots in Figure 6 using the LDGRF durations from Share et al. (2018), Winter et al. (2018), and Ajello et al. (2021) have quite different distributions with little evidence of the correlations evident using the Gopalswamy et al. (2019) parameters. Given the statistical limitations, at most, Figure 6 suggests that the longest-duration LDGRFs tend to be associated with the longest deca-hectometric (DH) type II bursts or lowest end frequencies, whereas LDGRFs can also have a range of durations for a given type II duration or end frequency. Furthermore, any notable relationship disappears by removing the longest-duration point (2012 March 7), as confirmed by the low values of the rank correlation coefficients. It should be noted that the samples analyzed by Share et al. (2018) and Winter et al. (2018; limited to before 2015) do not include the two long-duration events on 2017 September 6 and 10 considered by Gopalswamy et al. (2019) and Ajello et al. (2021); nevertheless, adding these points to the corresponding scatter plot (using the values computed by Gopalswamy et al. 2019 or Ajello et al. 2021) does not cause any appreciable improvement in the correlation. We conclude that the strong relationships between type II radio emissions and LDGRF durations reported by Gopalswamy et al. (2018a) are not evident using independent estimates of the LDGRF durations from three other studies and might be caused by the selection of events with a >3 hr duration along with a less accurate approach in the analysis of LAT data (uncertainties on LDGRF durations and onset times).

4. Discussion and Conclusions

In this work, we have investigated the uncertainties associated with the estimates of the >500 MeV populations of interacting protons producing the high-energy γ-ray emission in LDGRFs and escaping protons in interplanetary space associated with SEP events. This relationship potentially provides a test of whether the back-precipitation of SEP protons accelerated by CME-driven shocks is able to account for the measured γ-ray emission. In particular, in view of their significant implications on the LDGRF origin, we have reanalyzed the calculation by de Nolfo et al. (2019) of the number of high-energy SEPs for a sample of 14 SEP events

[6] For comparison with the photon arrival times measured at the observer's distance (1 au), the derived release times account for an 8 minute delay.

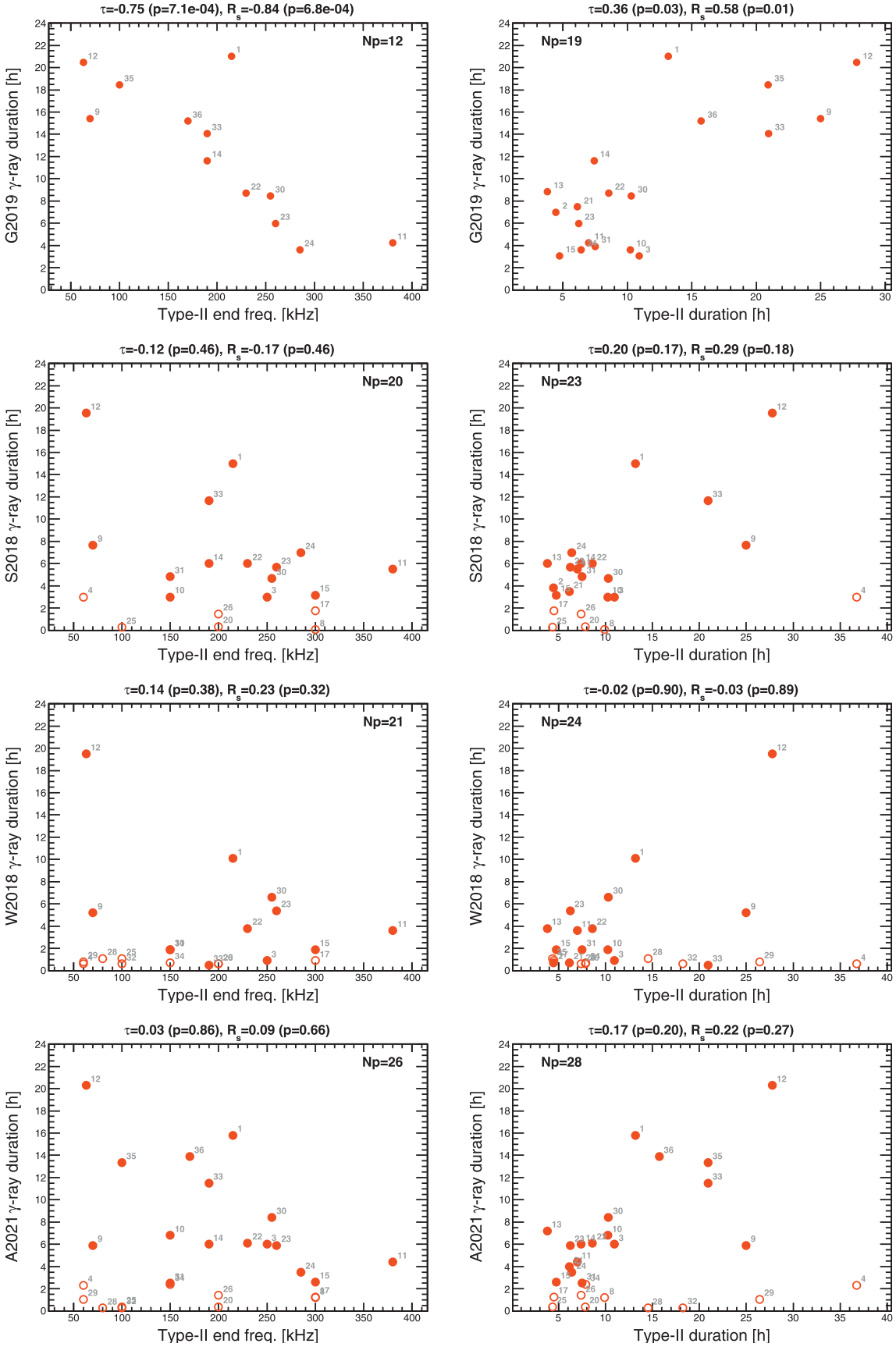

Figure 6. Scatter plots of the LDGRF duration as a function of the type II end frequency (left panels) and duration (right panels). From top to bottom: calculations using results from Gopalswamy et al. (2019, G2019), Share et al. (2018, S2018), Winter et al. (2018, W2018), and Ajello et al. (2021, A2021). The number of events used in each plot, along with the Kendall (τ) and Spearman (R_s) correlation coefficients (and corresponding p-values), are reported for each panel. The event numbers in Table 3 are given adjacent to the data points. The open markers indicate events not included by Gopalswamy et al. (2019).

observed at three spacecraft locations. We have reviewed the assumptions used to evaluate the proton numbers for these two populations, thereby testing their conclusion that there is no significant correlation between these numbers and confirming that they imply unrealistically high precipitation fractions. We have also explored the relationship between the durations of LDGRFs and type II radio emission reported by Gopalswamy et al. (2018a) using independent assessments of the LDGRF duration. The main conclusions can be summarized as follows.

1. We have examined the uncertainties associated with the different elements of the calculation and used conservative assumptions to estimate the lower limits on the precipitation fractions. In particular, we have removed the correction introduced by Share et al. (2018) that assumed an isotropic distribution for the downward propagating protons producing the LDGRFs. Furthermore, we have developed a new method to compute the >500 MeV SEP spatial distribution based on experimental constraints, and we have discussed the effect of the choice of the latitudinal angle describing the SEP propagation axis using both the parent flare locations and the CME directions from different data sets. We have shown that, even in the most favorable case, the $N_{\rm LDGRF}$ and $N_{\rm SEP}$ numbers are only poorly/moderately correlated. Most importantly, although the corresponding precipitation fractions are often substantially lower than those computed by de Nolfo et al. (2019), the values obtained for several events are still too high (>20%) to be compatible with current theories of a CME-shock origin of LDGRFs that predict a maximum P_N value of ∼2% (Hudson 2018; Klein et al. 2018; Hutchinson et al. 2022).
2. For the number of >500 MeV interacting protons, we used the estimates provided by Share et al. (2018) and, more recently, Ajello et al. (2021). Overall, the two calculations are in reasonable agreement, although P_N is higher for a couple of events in the latter case, supporting the lack of a highly significant correlation with the $N_{\rm SEP}$ numbers and the high precipitation fractions that challenge the CME-shock scenario.
3. We also note that even larger precipitation fractions would be required for more turbulent interplanetary conditions or if $N_{\rm LDGRF}$ is underestimated when corrections for occultation effects are made for near- or behind-the-limb eruptions (Gopalswamy et al. 2021).
4. In addition, we have investigated the relationship between the duration of LDGRFs and the duration and end frequency of the concomitant interplanetary type II radio emission. We have found that the high correlation levels obtained by Gopalswamy et al. (2018a, 2019) are reduced when we use the LDGRF durations from independent analyses by Share et al. (2018), Winter et al. (2018), and Ajello et al. (2021) and when events with durations of less than 3 hr, excluded by Gopalswamy et al. (2018a, 2019), are included.

Furthermore, we note that the direct link between the time histories of long-duration γ-ray and interplanetary type II emissions is not obvious. In particular, while LDGRFs are mostly produced by >300 MeV protons accelerated close to the Sun, type II radio emission is initiated by the acceleration at shocks of low-energy electrons (e.g., Bale et al. 1999). Since the emission occurs at the plasma frequency, which decreases with heliocentric distance, a lower end frequency implies that type II emission was produced by the shock out to larger distances from the Sun. The correlations found by Gopalswamy et al. (2018a) therefore suggest that the longest-duration LDGRFs are associated with CME shocks that produce type II radio bursts out to larger heliocentric distances. Since type II emission is taken as an indicator that the shock is accelerating particles, the correlation between the type II and LDGRF emission durations appears to be consistent with the scenario in which the precipitation of shock-accelerated protons generates the LDGRF. However, as noted above, the fraction of precipitating protons in the CME-shock paradigm is predicted to drastically decrease with increasing shock distances due to the magnetic mirroring effect (Hutchinson et al. 2022). For example, the ∼190 kHz ending frequency in the 2015 June 21 event corresponds to ∼90 $R_\odot$ (Gopalswamy et al. 2018a), while in several cases, the type II emission continues until the shocks reach the observing spacecraft at 1 au. Hence, it is not obvious why more extended type II bursts and a lower end frequency should be correlated with the LDGRF duration. Furthermore, evidence for the continuous acceleration of >300 MeV protons by CME-driven shocks moving out through the inner heliosphere is lacking. Since faster CME-driven shocks typically accelerate particles over larger heliodistances, the relationship with DH radio bursts could be just a reflection of the association of LDGRFs with relatively fast CMEs. Consequently, the fraction of precipitating protons in the CME-shock paradigm is predicted to drastically decrease with increasing shock distances due to the magnetic mirroring effect, exacerbating the problem for fast CMEs (Hutchinson et al. 2022).

In general, back-precipitation is also disfavored by the presence of the CME structure following the shock (e.g., Zurbuchen & Richardson 2006), which potentially complicates the path of particles propagating from the shock to the Sun. In fact, although magnetic field lines in the CME may be rooted at the Sun and might provide a conduit for particles to precipitate back to an extended region around the solar event, there are two issues with this scenario. First, magnetic mirroring must still be overcome, and the generally low magnetic field fluctuation levels in interplanetary CMEs will likely reduce the level of particle scattering. Second, field lines passing through the shock do not enter the CME, and observations typically show a significant energy-dependent drop in the particle intensity between the shock and the interior of the CME (e.g., Sanderson et al. 2003). Thus, we would expect only a fraction of the particles accelerated at the shock to enter the CME. In addition, the sheath region behind a shock is typically turbulent and is known to inhibit the propagation of galactic cosmic rays in Forbush decreases. Therefore, the propagation of high-energy particles from the shock is likely to be restricted by the sheath. Thus, we would expect these model calculations to overestimate the number of back-precipitating protons that might be expected in the presence of CME-related structures following the shock.

These analyses of whether LDGRFs may be accounted for by the CME-shock paradigm are based on assessing correlations between physical parameters, but a strong correlation does not necessarily imply a causal connection. In fact, while one would expect a significant statistical relationship between LDGRFs and shock-related phenomena in the CME-shock hypothesis, even a high correlation between the interacting and interplanetary ion populations would not necessarily

demonstrate that they are both of CME-shock origin. We have shown that even when making conservative assumptions when estimating $N_{\rm LDGRF}$ and $N_{\rm SEP}$, the precipitation fractions for some events remain high and are inconsistent with models of proton back-precipitation. This analysis strongly suggests that the computed number of high-energy SEPs appears to be greatly insufficient for producing the observed γ-ray emission. We also note that most energetic SEP events measured at 1 au may include a direct contribution of flare-accelerated particles, as suggested by several authors (e.g., Grechnev et al. 2008; McCracken et al. 2008; Masson et al. 2009; Kahler et al. 2017; Kocharov et al. 2020). If so, the estimated P_N values—based on a pure shock acceleration particle origin—would be further underestimated.

As also suggested by the reduction in the correlation between the γ-ray and interplanetary type II radio emissions when including events with a duration of <3 hr, the apparent relationship (with clear exceptions) between LDGRFs and the interplanetary radio emission, as well as the CME speed/width and the SEP event size—as already noted by Share et al. (2018)—might just be a manifestation of the so-called "big flare syndrome" (Kahler 1982); i.e., energetic phenomena are statistically more likely to occur together in large solar eruptions even when there is no specific physical process relating them. For example, the duration of the LDGRF emission is also moderately correlated with the hard and soft X-ray durations of the associated solar flare emissions, although they originate from unrelated processes. Similarly, faster CMEs tend to be associated with more intense flares.

A natural alternative to the CME-shock scenario is represented by the flare-loop model (Ryan & Lee 1991; Mandzhavidze & Ramaty 1992; Chupp & Ryan 2009; Grechnev et al. 2018; Ryan & de Nolfo 2018; de Nolfo et al. 2019; Ryan et al. 2019; de Nolfo et al. 2021). If particles are produced and injected on closed field lines, all of them will tend to precipitate on the solar atmosphere after a relatively long residence time associated with particle trapping and second-order Fermi acceleration. In addition, large ($\gtrsim 1\ R_\odot$) coronal loops can easily explain the extended γ-ray emission observed for behind-the-limb events. Thus, if we decouple the two energetic particle populations, as the data suggest, we are apparently restricted to an acceleration/transport process that must operate close to the Sun for extended periods of time. However, such models have been discussed in the literature for a loop-based acceleration/trapping process that must be further explored.

Acknowledgments

A.B., G.A.D., and I.G.R. acknowledge support from NASA programs NNH19ZDA001N-HSR and NNH19ZDA001N-LWS. S.D. acknowledges support from the UK STFC through grant ST/V000934/1 and NERC through grant NE/V002864/1. The authors also thank the anonymous reviewer whose comments helped to improve and clarify this manuscript.

Data Availability

The DONKI catalog (https://ccmc.gsfc.nasa.gov/donki/) is compiled at the Community Coordinated Modeling Center (CCMC) by NASA. The CDAW SOHO/LASCO CME catalog (https://cdaw.gsfc.nasa.gov/CME_list/) is generated and maintained at the CDAW Data Center by NASA and the Catholic University of America in cooperation with the Naval Research Laboratory. The catalog of type II radio bursts observed by Wind/WAVES can be found at https://cdaw.gsfc.nasa.gov/CME_list/radio/waves_type2.html. The Lockheed-Martin SolarSoft system is available at the LMSAL website (http://www.lmsal.com/solarsoft/).

ORCID iDs

A. Bruno https://orcid.org/0000-0001-5191-1662
G. A. de Nolfo https://orcid.org/0000-0002-3677-074X
J. M. Ryan https://orcid.org/0000-0003-3534-5968
I. G. Richardson https://orcid.org/0000-0002-3855-3634
S. Dalla https://orcid.org/0000-0002-7837-5780

References

Ackermann, M., Allafort, A., Baldini, L., et al. 2017, ApJ, 835, 219
Ajello, M., Baldini, L., Bastieri, D., et al. 2021, ApJS, 252, 13
Akimov, V. V., Ambrož, P., Belov, A. V., et al. 1996, SoPh, 166, 107
Bale, S. D., Reiner, M. J., Bougeret, J. L., et al. 1999, GeoRL, 26, 1573
Bruno, A. 2017, SpWea, 15, 1191
Bruno, A., Bazilevskaya, G. A., Boezio, M., et al. 2018, ApJ, 862, 97
Bruno, A., & Richardson, I. G. 2021, SoPh, 296, 36
Chupp, E. L., & Ryan, J. M. 2009, RAA, 9, 11
Cliver, E. W., Kahler, S. W., & Vestrand, W. T. 1993, ICRC (Calgary), 3, 91
Dalla, S., de Nolfo, G. A., Bruno, A., et al. 2020, A&A, 639, A105
de Nolfo, G., Bruno, A., Ryan, J., et al. 2021, ICRC (Madison, WI), 358
de Nolfo, G. A., Bruno, A., Ryan, J. M., et al. 2019, ApJ, 879, 90
Ellison, D. C., & Ramaty, R. 1985, ApJ, 298, 400
Gopalswamy, N., Mäkelä, P., Yashiro, S., et al. 2015, JPhCS, 642, 012012
Gopalswamy, N., Mäkelä, P., Yashiro, S., et al. 2018a, ApJL, 868, L19
Gopalswamy, N., Yashiro, S., Mäkelä, P., et al. 2018b, ApJL, 863, L39
Gopalswamy, N., Mäkelä, P., Yashiro, S., et al. 2019, JPhCS, 1332, 012004
Gopalswamy, N., Mäkelä, P., Yashiro, S., et al. 2020, ApJL, 295, 18
Gopalswamy, N., Xie, H., Akiyama, S., Mäkelä, P., & Yashiro, S. 2014, EP&S, 66, 104
Gopalswamy, N., Xie, H., Mäkelä, P., et al. 2013, AdSpR, 51, 1981
Gopalswamy, N., Xie, H., Yashiro, S., et al. 2012, SSRv, 171, 23
Gopalswamy, N., Yashiro, S., Mäkelä, P., Xie, H., & Akiyama, S. 2021, ApJ, 915, 82
Gopalswamy, N., Yashiro, S., Michalek, G., et al. 2010, SunGe, 5, 7
Grechnev, V. V., Kiselev, V. I., Kashapova, L. K., et al. 2018, SoPh, 293, 133
Grechnev, V. V., Kurt, V. G., Chertok, I. M., et al. 2008, SoPh, 252, 149
Hudson, H. S. 2018, in IAU Symp. 335, Space Weather of the Heliosphere: Processes and Forecasts, ed. C. Foullon & O. E. Malandraki (Cambridge: Cambridge Univ. Press), 49
Hutchinson, A., Dalla, S., Laitinen, T., et al. 2022, A&A, 658, A23
Jin, M., Petrosian, V., Liu, W., et al. 2018, ApJ, 867, 122
Kahler, S. W. 1982, JGRA, 87, 3439
Kahler, S. W., Cliver, E. W., & Kazachenko, M. 2018, ApJ, 868, 81
Kahler, S. W., Kazachenko, M., Lynch, B. J., & Welsch, B. T. 2017, JPhCS, 900, 012011
Klein, K.-L., Tziotziou, K., Zucca, P., et al. 2018, in Solar Particle Radiation Storms Forecasting and Analysis, ed. O. E. Malandraki & N. B. Crosby (Cham: Springer), 133
Kocharov, L., Laitinen, T., Vainio, R., et al. 2015, ApJ, 806, 80
Kocharov, L., Pesce-Rollins, M., Laitinen, T., et al. 2020, ApJ, 890, 13
Koldobskiy, S., Usoskin, I., & Kovaltsov, G. A. 2022, JGRA, 127, e29919
Kouloumvakos, A., Rouillard, A. P., Share, G. H., et al. 2020, ApJ, 893, 76
Lario, D., Wijsen, N., Kwon, R. Y., et al. 2022, ApJ, 934, 55
Mandzhavidze, N., & Ramaty, R. 1992, ApJ, 389, 739
Masson, S., Klein, K. L., Bütikofer, R., et al. 2009, SoPh, 257, 305
McCracken, K. G., Moraal, H., & Stoker, P. H. 2008, JGRA, 113, A12101
Mishev, A. L. 2023, JASTP, 243, 106021
Mishev, A. L., Velinov, P. I. Y., Mateev, L., & Tassev, Y. 2012, JASTP, 89, 1
Murphy, R. J., Dermer, C. D., & Ramaty, R. 1987, ApJS, 63, 721
Paassilta, M., Raukunen, O., Vainio, R., et al. 2017, JSWSC, 7, A14
Pesce-Rollins, M., Omodei, N., Petrosian, V., et al. 2015, ApJL, 805, L15
Plotnikov, I., Rouillard, A. P., & Share, G. H. 2017, A&A, 608, A43
Ramaty, R., Murphy, R. J., & Dermer, C. D. 1987, ApJL, 316, L41
Reames, D. V. 2009, ApJ, 706, 844

Richardson, I. G., von Rosenvinge, T. T., & Cane, H. V. 2015, SoPh, 290, 1741
Ryan, J., De Nolfo, G. A., & Gary, D. 2019, ICRC (Madison, WI), 36, 1144
Ryan, J. M. 2000, SSRv, 93, 581
Ryan, J. M., & de Nolfo, G. 2018, 42nd COSPAR Scientific Assembly, D2.1–20–18
Ryan, J. M., & Lee, M. A. 1991, ApJ, 368, 316
Sanderson, T. R., Marsden, R. G., Tranquille, C., et al. 2003, GeoRL, 30, 8036
Share, G. H., Murphy, R. J., White, S. M., et al. 2018, ApJ, 869, 182
Thernisien, A. 2011, ApJS, 194, 33
Vashenyuk, E. V., Balabin, Y. V., & Gvozdevsky, B. B. 2011, ASTRA, 7, 459
Verbeke, C., Mays, M. L., Kay, C., et al. 2022, AdSpR,
Vilmer, N., MacKinnon, A. L., & Hurford, G. J. 2011, SSRv, 159, 167
Waterfall, C. O. G., Dalla, S., Laitinen, T., Hutchinson, A., & Marsh, M. 2022, ApJ, 934, 82
Wild, J. P., Smerd, S. F., & Weiss, A. A. 1963, ARA&A, 1, 291
Winter, L. M., Bernstein, V., Omodei, N., & Pesce-Rollins, M. 2018, ApJ, 864, 39
Xie, H., Mäkelä, P., Gopalswamy, N., & St. Cyr, O. C 2016, JGRA, 121, 6168
Zurbuchen, T. H., & Richardson, I. G. 2006, SSRv, 123, 31